ADVANCED FUNCTIONAL MATERIALS
www.afm-journal.de

MaterialsViews
www.MaterialsViews.com

Dramatic Activity of $C_3N_4/BiPO_4$ Photocatalyst with Core/Shell Structure Formed by Self-Assembly

*Chengsi Pan, Jing Xu, Yajun Wang, Di Li, and Yongfa Zhu**

Core/shell structured $C_3N_4/BiPO_4$ photocatalyst is fabricated via a facile ultrasonic dispersion method. The thickness of the shell may be controlled by tuning the amount of C_3N_4 in the dispersion, which determines the enhanced level of photocatalytic activity. The optimum photocatalytic activity of C_3N_4/$BiPO_4$ at a weight ratio of 4% ($C_3N_4/BiPO_4$) under UV irradiation is almost 4.5 times as high as that of reference P25 (TiO_2) and 2.5 times of $BiPO_4$. More attractively, the dramatic visible light photocatalytic activity is generated due to the C_3N_4 loaded. The enhancement in performance is demonstrated to be the match of lattice and energy level between the C_3N_4 and $BiPO_4$. This match facilitates the separation and transfer of photogenerated electron–hole pairs at the heterojunction interfaces and may be important for other core/shell structured materials. In addition, this method is expected to be extended for other C_3N_4 loaded materials.

1. Introduction

The photocatalytic technology has attracted much attention due to its potential use in organic wastewater treatment for environmental remediation.[1] Nevertheless, the most widely used photocatalyst, TiO_2, suffers from two main problems, which include the low solar energy conversion efficiency and the high recombination of photogenerated electron–hole pairs.[2] Therefore, the performance of TiO_2 does not meet the needs of industrial applications and, as a result, the development of new efficient photocatalytic systems is still in progress.

Among all photocatalysts, hetero-nanostructured catalysts become increasingly attractive and include Ag/TiO_2, Graphite/ZnO and Ag/AgCl.[3a–c] For this type of photocatalysts, different materials can be integrated within the same structure so that multiple functionalities may be incorporated.[3d] In spite of extensive research in the past, efficient hetero-nanostructured photocatalysts with high photocatalytic activity (compared to the commercial TiO_2, P25), good stability, and low cost are still rare. There are two important factors to be considered: one is the suitable conduction and valance band levels promoting charge separation at the heterojunction interfaces; the other is the lattice match between the two components so that the core/shell structures remain stable during the catalytic reaction.

In the past five years, a series of π-conjugated material/photocatalyst core/shell structures such as graphite/TiO_2, C_{60}/ZnO, and polyaniline(PANI)/ZnO have been demonstrated to improve photocatalytic properties.[4] These π-conjugated materials have also been regarded as able to increase separation efficiency of photogenerated electron–hole pairs through the formation of electronic interactions with photocatalysts during the catalytic reaction. The graphite-like carbon nitride (g-C_3N_4), as one of the π-conjugated materials, has recently been reported to possess the performance of hydrogen or oxygen production from water splitting and organic degradation under visible light irradiation.[5] Different from the inorganic π-conjugated materials (e.g., graphite and C_{60}), g-C_3N_4 is a soft polymer so that it can easily coat on other compounds' surface. On the other hand, different from organic π-conjugated materials such as PANI, g-C_3N_4 is often well-crystallized due to the nature of the lamellar structure, which facilitates the charge transfer.[6] As a result, this conjugated material may be an excellent coating for the transport of the photogenerated carriers. Some photocatalysts loaded with this CN polymer like TiO_2 and N-Doped $H_2Ta_2O_6$ has exhibited superior photocatalytic activity.[7] However, the microstructure control of these composites has not been achieved, and thus the carrier transfer between heterojunction interfaces is far from efficiency. Therefore, from this point of view, the design of core/shell structures between C_3N_4 and an appropriate photocatalyst remains a challenge. In addition, understanding this system is important for the future development of photocatalysts and photoelectric devices.

$BiPO_4$, an oxoacid salt photocatalyst, was discovered by our group and exhibits more attractive activity than that of P25.[8] To the best of our knowledge, few efforts have been made to electronically combine conjugated materials such as g-C_3N_4 with this type of photocatalyst. Here, the $C_3N_4/BiPO_4$ core/shell structure is synthesized through a self-assembly method. The interaction between $BiPO_4$ and g-C_3N_4 as well as the resulting effect on photocatalytic activity is investigated systematically.

2. Results and Discussion

2.1. Structure and Morphology of $C_3N_4/BiPO_4$

The formation of g-$C_3N_4/BiPO_4$ core/shell structures involves a two step process (**Scheme 1**). First, g-C_3N_4 is exfoliated into

---

Dr. C. Pan, J. Xu, Y. Wang, D. Li, Prof. Y. F. Zhu
Department of Chemistry
Tsinghua University
Beijing, 100084, P. R. China
E-mail: zhuyf@mail.tsinghua.edu.cn

DOI: 10.1002/adfm.201102306

Scheme 1. Schematic illustration of the preparation of the $C_3N_4/BiPO_4$ core/shell structure.

sheet structures through an ultrasonic method in CH_3OH solvent. Second, the as-prepared $BiPO_4$ nanorods[8a] are added into the suspension, and then these g-C_3N_4 sheets will spontaneously coat on the nanorods to achieve a minimum surface energy. The shell thickness can be tuned by simply increasing or decreasing the g-C_3N_4 content.

An estimate of the g-C_3N_4 content in the $C_3N_4/BiPO_4$ core/shell nanostrucutres (CNBP) was obtained by thermogravimetric analysis (TGA). For example, the C_3N_4 content of sample CNBP-10 is calculated to be approximately 9.0 wt% (Supporting Information Figure S1). For $C_3N_4/BiPO_4$ samples, two weight loss regions can be seen in the TG curve. A slight weight loss (≈0.5%) is observed before 290 °C, indicating the desorption of water. Major weight loss commences at 300 °C and lasts until 650 °C, which can be attributed to the burning of g-C_3N_4. The g-C_3N_4 content of the samples is more or less the same as the one calculated from the experimental charge, and is therefore increasing with the mass ratio of g-C_3N_4 (**Table 1**). Also, as reported in Table 1, the g-C_3N_4 shell becomes thicker with an increase in the g-C_3N_4:$BiPO_4$ mass ratio.

The X-ray diffraction (XRD) patterns of $C_3N_4/BiPO_4$ prepared with different mass ratios of C_3N_4 to $BiPO_4$ is shown in the Supporting Information (Figure S2). The $C_3N_4/BiPO_4$ samples present a two-phase composition: C_3N_4 and $BiPO_4$ (JCPDS No. 08-0209). No impurity phase is emerged in the $C_3N_4/BiPO_4$ samples. Two pronounced peaks are found in Figure S2b (Supporting Information) at 27.4° and 13.2°, corresponding to the characteristic interplanar staking peak of aromatic systems and the interlayer structural packing, respectively, which is consistent with the XRD pattern reported in the literature.[9] With increasing the C_3N_4 content, the (002) peak of C_3N_4 becomes sharper, which implies the crystallization of the coating layers becomes better.

Figure 1 shows transmission electron microscopy (TEM) images of CNBP composites prepared with different mass ratios of C_3N_4 to $BiPO_4$. As can be seen from the images, the $BiPO_4$ nanorods are surrounded by C_3N_4 shells. Figure 1a shows that after ultrasonic treatment C_3N_4 is exfoliated into sheet structures with rolled edges. Figure 1b shows the morphology of CNBP-1, which is prepared with 1% mass ratio of C_3N_4 to $BiPO_4$. The C_3N_4 shell is very thin at this resolution and some places are not completely coated. As shown in Figure 1c, for CNBP-4, the C_3N_4 shell is thicker, ≈8 nm, while for CNBP-10, it is about 15–30 nm thick (Figure 1d). Hence, the thickness of the C_3N_4 shells increases with increasing the mass ratio of C_3N_4 to $BiPO_4$. This is because C_3N_4 can be exfoliated into thin sheets under experimental conditions. These soft sheets then coat on $BiPO_4$ cores to achieve a minimum surface energy.

Table 1. Physicochemical characterization of $C_3N_4/BiPO_4$ (CNBP) samples.

Sample	$C_3N_4/BiPO_4$ [wt%]	C_3N_4 content [wt%]	Thickness of C_3N_4 [nm]	S_{BET} [m^2 g^{-1}]
$BiPO_4$	0	0	0	3.0
CNBP-1	1%	1.0%	0–5	3.1
CNBP-2	2%	1.9%	3–5	3.2
CNBP-3	3%	2.9%	5–8	3.2
CNBP-4	4%	3.8%	7–10	3.2
CNBP-5	5%	4.7%	10–15	3.3
CNBP-10	10%	9.0%	15–30	3.5

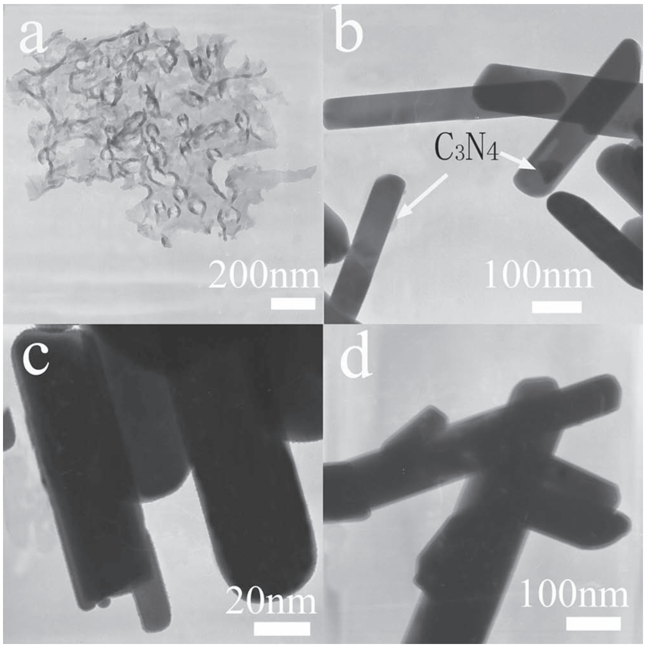

Figure 1. TEM images of a) C_3N_4 sheets after ultrasonic treatment and the CNBP samples: b) CNBP-1, c) CNBP-4, and d) CNBP-10.

Figure 2 shows the scanning electron microscopy (SEM) images of CNBP-10 core/shell nanostructures in comparison with pre-synthesized $BiPO_4$ and pure C_3N_4. It can be seen that at the beginning C_3N_4 samples are irregular particles consisting of lamellar structures, while $BiPO_4$ nanorods have obvious edges (Figure 2a,b). After coated with C_3N_4, no obvious uncoated C_3N_4 nanoparticles are observed (Figure 2c), which implies that the coating behavior of C_3N_4 is general, and not only occurring on some special nanorods. Additionally, all trunks of the final nanorods become round and therefore the diameter increases significantly compared to the size of the initially coated materials (Figure 2d).

Figure 3a,b shows the dark and bright field TEM images of sample CNBP-10. It can be seen clearly that there is a smooth coating layer on the surface of $BiPO_4$. Figure 3c,d shows high-resolution TEM images of sample CNBP-10, which was used to estimate C_3N_4 shell thickness and to show details of the coating structures. The thickness of the C_3N_4 layer coated on the CNBP-10 is about 18 nm, and the interpart boundary of the as-prepared sample was distinctly different from the $BiPO_4$

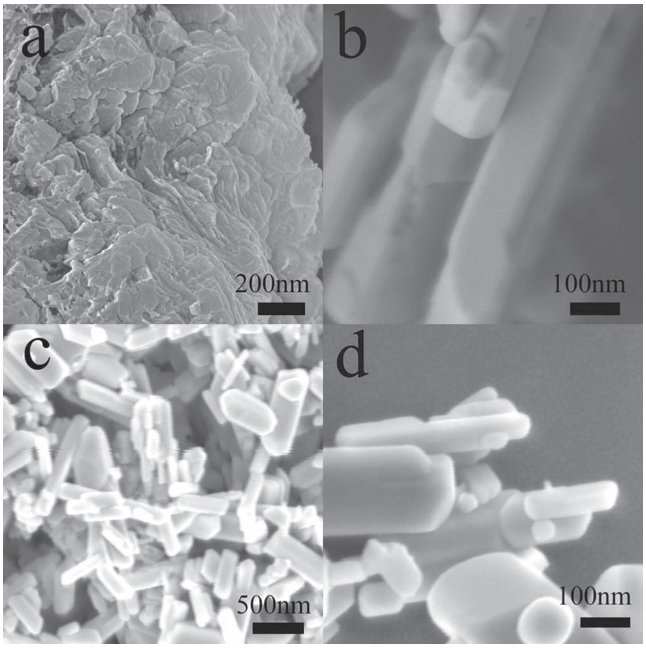

Figure 2. SEM images of a) C_3N_4 without ultrasonic treatment, b) $BiPO_4$ nanorods before coating, c) CNBP-10, and d) the magnified image of (c).

core. As can be seen from Figure 3, the lattice structure of C_3N_4 was very orderly and also different from the $BiPO_4$ lattice. The $BiPO_4$ nanorods contain (100) planes perpendicular to the axis while (011) planes along the axis as shown in Figure 3d and previously reported.[8a] On the other hand, for C_3N_4 layers, the measured interplanar spacing is 0.325 nm which corresponds to the C_3N_4 (002) plane. HRTEM images for CNBP-1 and CNBP-4 are also supplied in Supporting Information Figure S3. In Figure S3, the interface can be easily indentified from the terminated defects across the nanorods. In addition, C_3N_4 shows an obviously improved crystallinity with increasing its content.

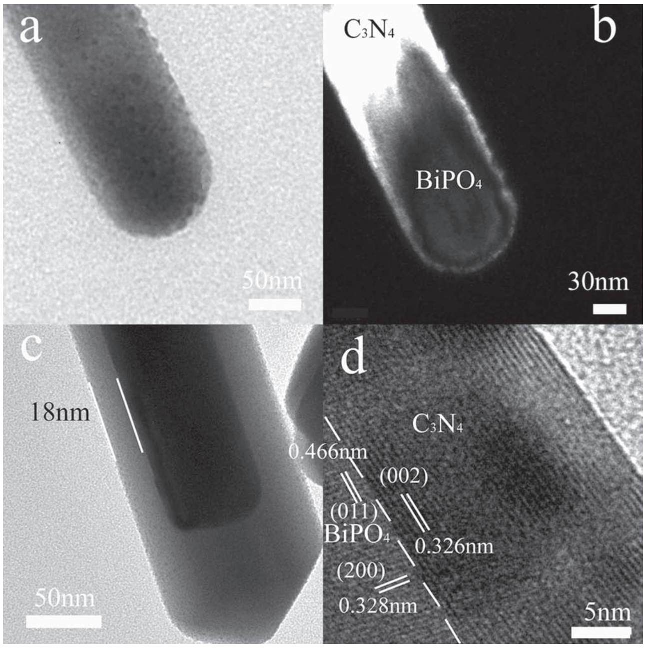

Figure 3. Bright field TEM (a), dark field TEM (b), and HRTEM images (c,d) of CNBP-10.

The optical properties of the CNBP samples were examined with UV-vis diffuse reflectance spectroscopy (Supporting Information Figure S4). As expected, $BiPO_4$ shows its fundamental absorption sharp edge rising at 320 nm. Meanwhile the CNBP samples absorb in the visible light region due to the presence of C_3N_4 on the $BiPO_4$ surface. It is notable that compared with $BiPO_4$, the absorption edge of CNBP experiences a red-shift of about 100 nm. Additionally, it is noteworthy that there is an obvious positive correlation between C_3N_4 content and intensity changes observed for all the CNBP samples in the UV-vis spectra. This may be due to the reason that introduction of the C_3N_4 can possibly cause modifications of the fundamental formation process of electron-hole pairs during irradiation.[4a]

Figure 4 shows the X-ray photoelectron spectroscopy (XPS) data for CNBP-4 and CNBP-10 core/shell nanostructures compared to that of pure $BiPO_4$. The wide spectra (Figure 4a) of CNBP samples reveal the predominant presence of phosphate, bismuth, oxygen, nitrogen, and carbon. The content of phosphate and bismuth decreases from $BiPO_4$ to CNBP-10, while the content of nitrogen increases at the same time due to the C_3N_4 coating as shown in Figure 4a and **Table 2**. These results indicate a thicker and more homogeneous coverage of C_3N_4 forms onto $BiPO_4$ with increasing the C_3N_4 content. It is also noted that when compared CNBP-4 and CNBP-10 with the reported C_3N_4,[10] the binding energy of N1s shows a negative shift (Figure 4b). On the contrary, for Bi6s it exhibits a positive one (Figure 4c) as compared to the pure $BiPO_4$ or the records in the literature.[11] Meanwhile the binding energy of P2p remains unchanged (Figure 4d). These results show that the interaction between Bi and N atoms results in the coating of the C_3N_4, not the simply physical adsorption. To further confirm this interaction, IR spectra were recorded for CNBP-4, CNBP-10, C_3N_4, and $BiPO_4$ (Supporting Information Figure S5). One new peak for CNBP-4 and CNBP-10 appears at around 445 nm, which can be assigned to the stretching vibrations of Bi–N bond.[12] This interaction can be strengthened due to the lattice match between the C_3N_4 and $BiPO_4$ according to the TEM and X-ray diffraction (XRD) results, which are detailed in **Scheme 2**, and may induce the formation of the core/shell structure.

2.2. Photocatalytic Properties of C_3N_4/$BiPO_4$

The photoactivity of CNBP samples were evaluated by degradation of methylene blue (MB), a hazardous dye as well as a common model to test the photodegradation capability.[13] Supporting Information Figure S6a shows the MB photodegradation on the CNBP with different C_3N_4 content under UV light irradiation. The uncoated $BiPO_4$ and C_3N_4 are listed as references. All of the C_3N_4/$BiPO_4$ photocatalysts exhibit higher photocatalytic activity than the pure $BiPO_4$ under UV light irradiation. The activity of CNBP-4 is obviously superior to the others. After 5 min irradiation with UV light about 90% of MB is degraded in the presence of CNBP-4, while approximately

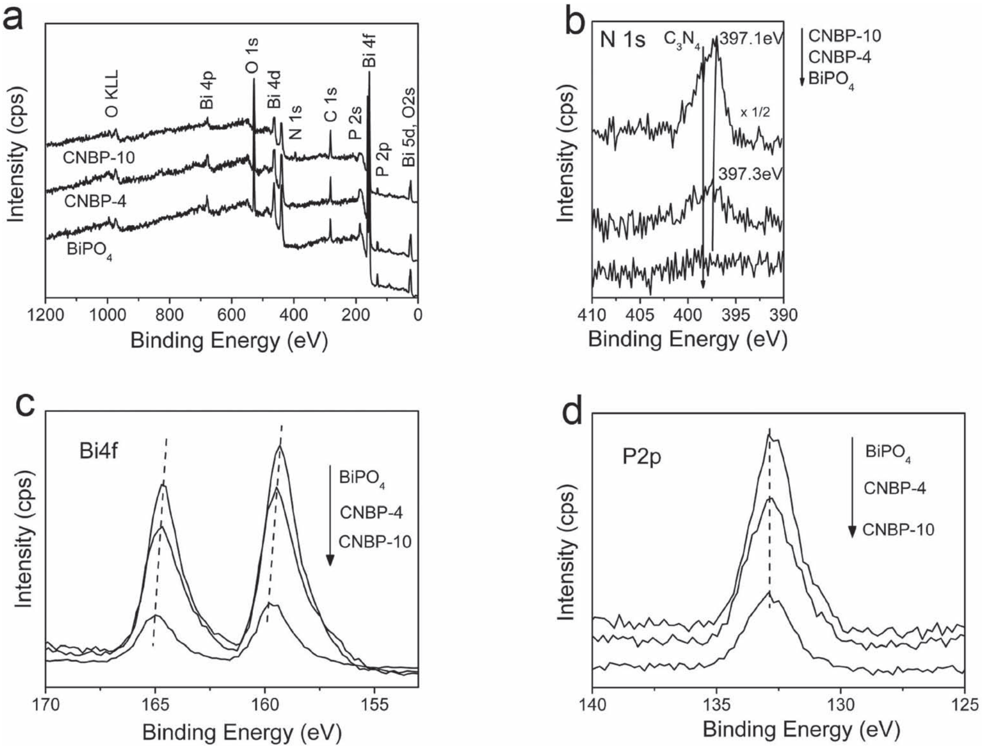

Figure 4. XPS spectra for CNBP samples: a) wide spectra, b) N1s, c) Bi4f, and d) P2p.

20 min is required to reach the same degradation level for P25 as reported by us before[8a] and 15min for pure $BiPO_4$. It is also noted that C_3N_4 shows a negligible MB degradation within 15 min of UV irradiation. To further depict the photocatalytic reaction, the photocatalytic degradation process was also fitted to pseudo-first-order kinetics, and the value of the rate constant k is equal to the corresponding slope of the fitting line, as can be seen in **Figure 5**a. The photocatalytic rate constant is sharply enhanced with increasing the C_3N_4 content. When the ratio of C_3N_4:$BiPO_4$ reaches 4% (CNBP-4), it exhibits the highest photocatalytic activity. The apparent rate constant k is 0.4701 min^{-1}, which is almost 4.5 times as high as that of P25[8a] and 2.5 times that of pure $BiPO_4$. However, as the proportion of C_3N_4 further increases, the degradation rate decreases gradually though it remains higher than that of $BiPO_4$. This change in UV activity of CNBP samples may be attributed to the excitation of $BiPO_4$. Although C_3N_4 shells are beneficial for charge transfer at heterojunction interfaces, they will shield UV light off of $BiPO_4$. Therefore, due to the demands of both the charge transfer and

Table 2. Atom concentration for N, Bi and P derived from XPS spectra.

Sample	N [at%]	Bi [at%]	P [at%]
$BiPO_4$	0	11.72	10.54
CNBP-4	3.22	9.54	8.93
CNBP-10	8.25	3.83	3.26

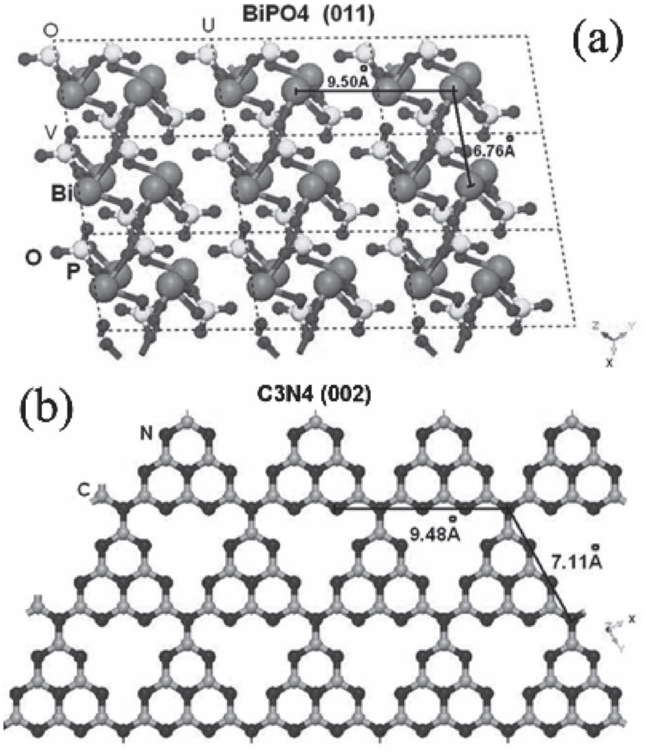

Scheme 2. Schematic illustration of the lattice match between (011) surface of $BiPO_4$ (a) and (002) surface of C_3N_4 (b).

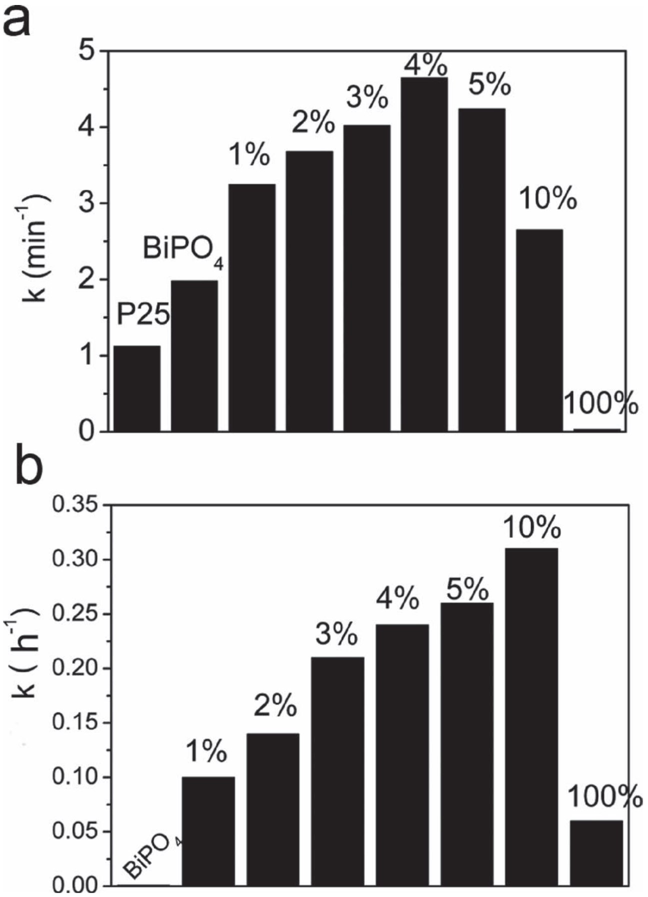

Figure 5. Apparent rate constants for the photodegradation of MB with UV irradiation (a) and with visible light ($\lambda > 420$ nm) irradiation (b) on CNBP samples with different weight ratio of C_3N_4 to $BiPO_4$. $BiPO_4$, C_3N_4, and P25 are shown as references.

light harvesting, our photocatalytic activity first increases and then decreases with the increasing thickness of C_3N_4, which results in the best photocatalytic activity of CNBP-4. The stability of the catalyst is also evaluated in the Supporting Information (Figure S7). It can be seen that after three cycles no obvious activity decrease for CNBP-4 occurs, and also no appreciable change in their overall morphologies has been observed after the catalytic reaction, which implies that the coating layers are rather stable.

The visible light photocatalytic activity of the C_3N_4/$BiPO_4$ photocatalysts was also evaluated by degradation of MB (Supporting Information Figure S6b) and *k*, calculated from the fitted curve, is shown in Figure 5b. Under visible light irradiation ($\lambda > 420$ nm), uncoated $BiPO_4$ has no notable effect on MB degradation, while the C_3N_4/$BiPO_4$ samples exhibit excellent visible light photocatalytic activity. Different from the UV activity, the visible light photocatalytic activity is enhanced gradually with the proportion of C_3N_4 increasing. When the ratio reaches to 10:100, the as-prepared photocatalyst has an optimal activity that can degrade MB by 85% in 6 h. It is noteworthy that the visible activities for CNBP samples are due to the excitation of C_3N_4. Increasing the thickness of C_3N_4 shell will not only benefit for charge transfer at the heterojunction interfaces, but also enhance the visible light absorption (Supporting Information Figure S4). As a result, the activity order for CNBP samples under visible light is different from that under UV light. It is interesting that the apparent *k* of CNBP-10 is 0.31 h^{-1}, which is also higher than that of C_3N_4 ($k = 0.06$ h^{-1}). This is probably because core/shell structures will not only decrease the charge recombination at heterojunction interfaces, but also suppress the aggregation of the C_3N_4 particles[14] and thus increase the surface area of C_3N_4.

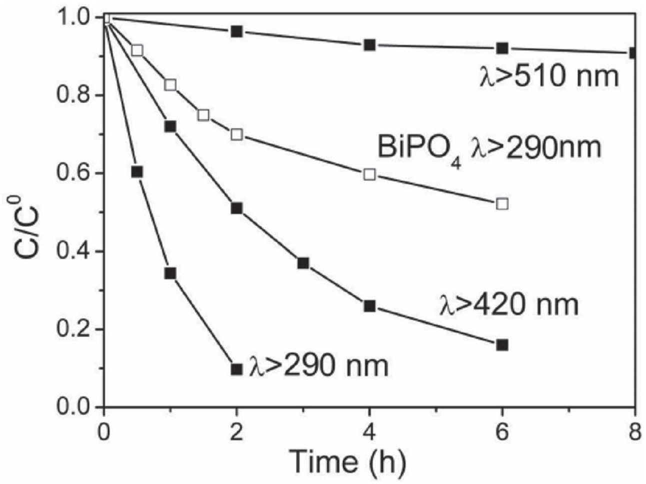

Figure 6. MB degradation on CNBP-10 at different cutoff wavelength. Xe lamp ($\lambda > 290$ nm) was used to simulate the sunlight. The MB degradation on $BiPO_4$ under Xe lamp irradiation is listed as a reference.

The influence of photosensitivity was also studied for CNBP-10 (**Figure 6**). The cutoff wavelength ($\lambda > 510$ nm) was used to evaluate the influence of photosensitivity. This cutoff wavelength ensures that only the MB, and not the CNBP, absorbs light. As shown in Figure 6, negligible degradation can be found on CNBP-10 when the cutoff wavelength is 510 nm. This suggests that the excitation of MB dye cannot sensitize the catalysts. The photocatalytic performances of CNBP-10 and pure $BiPO_4$ under simulated solar irradiation are also shown in Figure 6. In this work, a xenon lamp was used to simulate the solar irradiation. It shows that CNBP-10 has an obviously superior activity to the pure $BiPO_4$ under simulated solar irradiation and to itself under the visible light irradiation. The apparent *k* is 0.183 h^{-1}, which is comparable to that of Bi_2WO_6 (0.228 h^{-1}),[15] one of the best visible light photocatalysts we reported before.

The above results show that the loading amount of C_3N_4 has a great influence on the photocatalytic activity of the as-prepared catalysts. It may influence not only the separation of photogenerated electron-hole pairs discussed below, but also the light absorption. The photocatalytic activities with UV light, visible light, and simulated sunlight irradiation suggest the CNBP is an excellent photocatalyst candidate.

2.3. Mechanism of Photocatalytic Activity Enhancement

The above results show that the coating of C_3N_4 can enhance both UV and visible activity of $BiPO_4$. As is well known, this may be due to the high separation and transfer of photogenerated electron–hole pairs at the heterojunction interfaces. CNBP samples under UV illumination were chosen as an example to demonstrate this. In the case of visible light illumination, the situation may be similar except that it is C_3N_4 that absorbs light instead of $BiPO_4$.

As previous studies, the photocatalytic reactions could be regarded as an electrochemical process.[16] Supporting Information Figure S8a shows electrochemical impedance spectra (EIS) Nyquist plots of $BiPO_4$ and CNBP-4 electrodes before and after UV irradiation. The diameter of the arc radius on the EIS Nyquist plot of the CNBP-4 electrode is smaller than that of the $BiPO_4$ electrode regardless of whether with or without UV irradiation. This smaller the arc radius implies the higher the efficiency of charge transfer. Figure S8b (Supporting Information) shows the transient photocurrent responses via two on-off cycles of irradiation of C_3N_4, $BiPO_4$, and CNBP-4 electrodes, which may directly correlate with recombination efficiency of photogenerated carriers.[16] As shown in Figure S8b, a generation of photocurrent with good reproducibility for all samples is observed when samples are irradiated by UV light. This indicates that our electrode is stable and photoresponsive phenomenon is entirely reversible. The photocurrent densities of CNBP-4, $BiPO_4$, and C_3N_4 are 21.0, 8.1, and 2.2 μA cm^{-2}, respectively. This order is consistent with their photocatalytic activities. Thus, in the case of CNBP-4, the separation and transfer of photoinduced electron–hole pairs are more efficient through an interfacial interaction between C_3N_4 and $BiPO_4$.

The recombination of electron–hole pairs is also characterized by the lifetime of carriers. It can be reflected by the decays of PL transition centered on 550 nm excited at 254 nm as shown in **Figure 7**a. Moreover, the PL lifetime of three samples calculated by the exponential analysis is also shown in Figure 7a (inset). The PL lifetime decreases in the following order: CNBP-4 > $BiPO_4$ > C_3N_4. A longer PL lifetime means lower recombination rate of the electron–hole pairs, and thus higher photocatalytic activity.

This high separation efficiency may be due to the energy level match between C_3N_4 and $BiPO_4$. Theoretical calculations[5a] suggested that the highest occupied molecular orbital (HOMO) and lowest unoccupied molecular orbital (LUMO) potentials of g-C_3N_4 were –1.12 and 1.57 V, respectively. While the conduction band (CB) and valence band (VB) edge potentials of $BiPO_4$ were estimated to be –0.65 and 3.2 V, respectively, as reported previously.[8a] A scheme for the separation and transport of photogenerated electron–hole pairs at the $C_3N_4/BiPO_4$ interface is shown in Figure 7b. $BiPO_4$ can be excited by UV light and produce photogenerated electron–hole pairs. Since the VB position of $BiPO_4$ is lower than the HOMO of C_3N_4, the photogenerated holes on $BiPO_4$ can directly transfer to C_3N_4, making charge separation more efficient and reducing the probability of photogenerated electron–hole recombination, resulting in an enhanced photocatalytic activity. This effective separation of photogenerated electron–hole pairs driven by band potentials between two semiconductors, is also reported in other systems, such as C_3N_4/TaON.[17]

Furthermore, this high separation efficiency may be not only due to the heterojunction interfaces, but also due to the core/shell structure induced by the lattice match. This core/shell structure is supposed to favor the transport of both electrons and holes across individual $BiPO_4$ particle driven by strong dipolar fields arising from charged surface domains, as demonstrated in other core/shell structures, such as TiO_2/Ag and $BiFeO_3/SrTiO_3$.[18] These charged surface domains of $BiPO_4$ would, in effect, electrostatically drive the photoexcited electrons or holes from the core solids into the conduction and valence bands of shells.

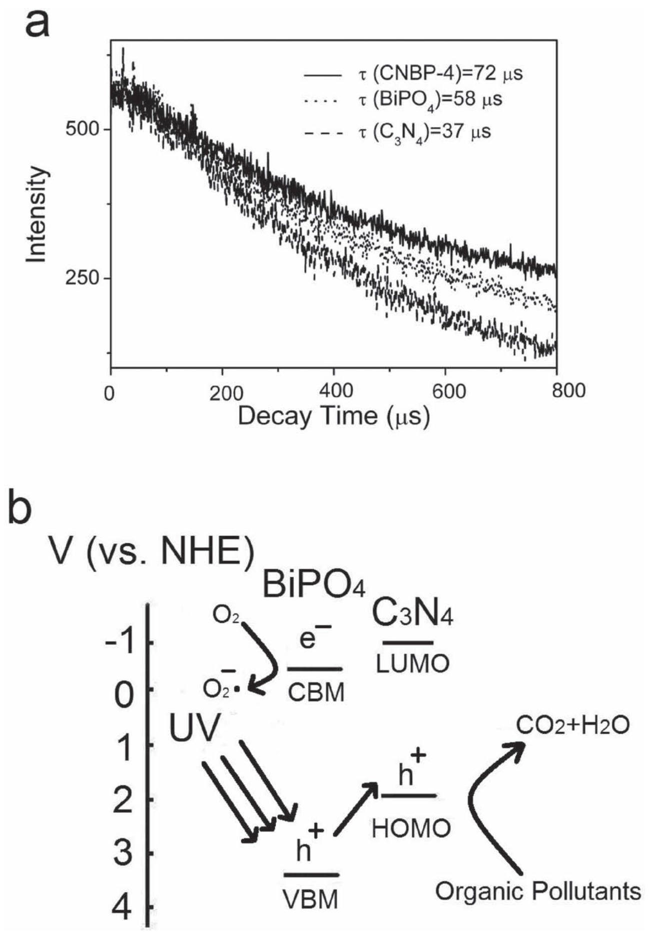

Figure 7. a) PL decay curves measured at λ_{ex} = 254 nm and λ_{em} = 550 nm for CNBP-4, $BiPO_4$, and C_3N_4. Inset shows the lifetime of carriers. b) Proposed energy levels of $BiPO_4$ and C_3N_4

3. Conclusions

A $C_3N_4/BiPO_4$ photocatalyst has been successfully synthesized via a facile ultrasonic dispersion method. After introduction of C_3N_4, the $C_3N_4/BiPO_4$ photocatalyst possessed significantly enhanced UV light photocatalytic activity and visible light photocatalytic activity. This enhancement has been demonstrated to be due to the high separation and easy transfer of photogenerated electron–hole pairs at the heterojunction interfaces derived from the match of lattice and energy level between the C_3N_4 and $BiPO_4$. This may be important for other core/shell structured photocatalysts and the method is expected to be extended for other C_3N_4 loaded materials.

4. Experimental Section

Synthesis: Melamine ($C_3H_6N_6$) was purchased from Sinopharm Chemical Reagent Corp, P. R. China; $BiPO_4$ (average particle size 400 nm × 80 nm) was synthesized according previously reported methods.[8a] All other reagents used in this research were analytically pure and used without further purification. The C_3N_4 used in this study was prepared by heating melamine to 550 °C for 2 h in N_2 atmosphere according to the literature.[19] The typical preparation of $C_3N_4/BiPO_4$ photocatalysts (CNBP) was as follows: first, an appropriate amount of C_3N_4 was added into methanol and then the beaker was placed in an ultrasonic bath for 30 min to completely disperse the C_3N_4. The $BiPO_4$ powder was added into the above solution and stirred in a fume hood for 24 h. After volatilization of the methanol, an opaque powder was obtained after drying at 100 °C. According to this method, different mass ratios of $C_3N_4/BiPO_4$ photocatalysts at 1%, 2%, 3%, 4%, 5%, and 10% were synthesized and named as CNBP-1, CNBP-2, CNBP-3,CNBP-4, CNBP-5, and CNBP-10, respectively.

Characterization: The products were characterized by powder XRD on a Bruker D8-advance X-ray diffractometer at 40 kV and 40mA for monochromatized Cu $K_{\alpha}1$ ($\lambda = 1.5406$ Å) radiation. Morphologies and structures of the prepared samples were further examined with a JSM 6301 electron scanning microscope and using TEM with a JEM 1010 electron microscope operated at an accelerating voltage of 100 kV. High-resolution TEM (HRTEM) images were obtained with a JEM 2010F field emission gun transmission electron microscope operated at an accelerating voltage of 200 kV. UV–vis diffuse reflectance spectra (DRS) of the samples were measured using Hitachi U-3010 UV–vis spectrophotometer. The Brunauer–Emmett–Teller (BET) specific surface area of the samples was characterized by nitrogen adsorption at 77 K with Micromeritics 3020. PL spectra were obtained using an Edinburgh Analytical Instruments FL/FSTCSPC920 coupled with a time correlated single-photon counting system. XPS spectra were measured in a PHI 5300 ESCA system. An Al K_{α} X-ray source with a power of 250 W was used. The pass energy of the analyzer was set at 37.25 eV, and the base pressure of the analysis chamber was better than 4×10^{-8} Torr (1 Torr = 133.3 Pa). The charge effect was calibrated using the binding energy of C1s.

Photocatalytic Evaluation: Photocatalytic activities of $BiPO_4$ were evaluated by degradation of MB under UV light irradiation of an 11 W low-pressure lamp at 254 nm. The average light intensity was 1.5 mW cm^{-2}. The visible light system for the photocatalytic reactions was composed of a 500 W xenon arc lamp and a cutoff filter ($\lambda > 420$ nm). The average light intensity during the visible light experiments was 31 mW cm^{-2}. The radiant flux was measured with a power meter from Institute of Electric Light Source (Beijing). MB solutions (100 mL, 10^{-5} mol L^{-1}) containing 0.050 g of samples were put in a glass beaker. Before the light was turned on, the solution was ultrasonicated for 10 min and then stirred for 30 min to ensure equilibrium between the catalysts. Three milliliters of sample solution were taken at given time intervals and separated through centrifugation (4000 rpm, 10 min). The supernatants were analyzed by recording variations of the absorption band maximum (664 nm) in the UV–vis spectra of MB using a U-3010 spectrophotometer (Hitachi).

Supporting Information

Supporting Information is available from the Wiley Online Library or from the author.

Acknowledgements

This work was partly supported by the National Natural Science Foundation of China (20925725 and 50972070) and National Basic Research Program of China (2007CB613303).

Received: September 27, 2011
Revised: December 7, 2011

[1] a) K. Hashimoto, H. Irie, A. Fujishima, Jpn. *J. Appl. Phys.* **2005**, *12*, 8269; b) M. R. Hoffmann, S. T. Martin, W. Choi, D. W. Bahnemann, *Chem. Rev.* **1995**, *95*, 69.

[2] a) A. L. Linsebigler, G. Lu, J. T. Yates, Jr., *Chem. Rev.* **1995**, *95*, 735; b) X. Chen, S. S. Mao, *Chem. Rev.* **2007**, *107*, 2891.

[3] a) I. Pastoriza-Santos, D. S. Koktysh, A. A. Mamedov, M. Giersig, N. A. Kotov, L. M. Liz-Marzán, *Langmuir* **2000**, *16*, 2731; b) L. W. Zhang, H. Y. Cheng, R. L. Zong, Y. F. Zhu, *J. Phys. Chem. C* **2009**, *113*, 2368; c) P. Wang, B. Huang, X. Qin, X. Zhang, Y. Dai, J. Wei, M. H. Whangbo, *Angew. Chem. Int. Ed.* **2008**, *47*, 7931; d) M. Li, X. F. Yu, S. Liang, X. N. Peng, Z. J. Yang, Y. L. Wang, Q. Q. Wang, *Adv. Funct. Mater.* **2011**, *21*, 1788.

[4] a) L. W. Zhang, H. B. Fu, Y. F. Zhu, *Adv. Funct. Mater.* **2008**, *18*, 2180; b) H. Zhang, R. L. Zong, J. C. Zhao, Y. F. Zhu, *Environ. Sci. Technol.* **2008**, *42*, 3803; c) H. Fu, T. Xu, S. Zhu, Y. F. Zhu, *Environ. Sci. Technol.* **2008**, *42*, 8064.

[5] a) X. C. Wang, K. Maeda, A. Thomas, K. Takanabe, G. Xin, J. M. Carlsson, K. Domen, M. Antonietti, *Nat. Mater.* **2009**, *8*, 76; b) X. C. Wang, K. Maeda, X. F. Chen, K. Takanabe, K. Domen, Y. D. Hou, X. Z. Fu, M. Antonietti, *J. Am. Chem. Soc.* **2009**, *131*, 1680.

[6] a) E. Kroke, M. Schwarz, E. Horath-Bordon, P. Kroll, B. Noll, A. D. Norman, *New J. Chem.* **2002**, *26*, 508; b) X. C. Wang, X. F. Chen, A. Thomas, X. Z. Fu, M. Antonietti, *Adv. Mater.* **2009**, *21*, 1609.

[7] a) X. Lu, Q. Wang, D. Cui, *J. Mater. Sci. Technol.* **2010**, *26*, 925; b) Q. Li, B. Yue, H. Iwai, T. Kako, J. Ye, *J. Phys. Chem. C* **2010**, *114*, 4100.

[8] a) C. S. Pan, Y. F. Zhu, *Environ. Sci. Technol.* **2010**, *44*, 5570; b) C. S. Pan, Y. F. Zhu, *J. Mater. Chem.* **2011**, *21*, 4235.

[9] F. Su, S. C. Mathew, G. Lipner, X. Fu, M. Antonietti, S. Blechert, X. Wang, *J. Am. Chem. Soc.* **2010**, *132*, 16299.

[10] a) Q. Guo, Y. Xie, X. Wang, S. Zhang, T. S. Hou, *Chem. Commun.* **2004**, 26; b) C.-B. Cao, Q. Lv, H.-S. Zhu, *Diamond Related Mater.* **2003**, *12*, 1070; c) M. Kim, S. Hwang, J. S. Yu, *J. Mater. Chem.* **2007**, *17*, 1656; d) G. Liu, P. Niu, C. Sun, S. C. Smith, Z. Chen, G. Q. Lu, H. M. Cheng, *J. Am. Chem. Soc.* **2010**, *132*, 11642.

[11] a) S. W. Ting, S. Cheng, K. Y. Tsang, N. V. D. Laak, K. Y. Chan, *Chem. Commun.* **2009**, 7333; b) J. Zhu, S. Wang, J. Wang, D. Zhang, H. Li, *Appl. Catal. B* **2011**, *102*, 120.

[12] A. Soran, H. J. Breunig, V. Lippolis, M. Arca, C. Silvestru, *Dalton Trans.* **2009**, 77.

[13] a) S. U. M. Khan, M. Al-Shahry, W. B. Ingler Jr., *Science* **2002**, *27*, 2243; b) K. H. Ji, D. M. Jang, Y. J. Cho, Y. Myung, H. S. Kim, Y. Kim, J. Park, *J. Phys. Chem. C* **2009**, *113*, 19966; c) L. W. Zhang, Y. J. Wang, H. Y. Cheng, W. Q. Yao, Y. F. Zhu, *Adv. Mater.* **2009**, *21*, 1286.

[14] X. Chen, Y. S. Jun, K. Takanabe, K. Maeda, K. Domen, X. Fu, M. Antonietti, X. Wang, *Chem. Mater.* **2009**, *21*, 4093.

[15] S. Zhu, T. Xu, H. Fu, J. Zhao, Y. Zhu, *Environ. Sci. Technol.* **2007**, *41*, 6234.

[16] a) H. Liu, Sh. Cheng, M. Wu, H. Wu, J. Zhang, W. Li, Ch. Cao, *J. Phys. Chem. A* **2000**, *104*, 7016; b) W. H. Leng, Z. Zhang, J. Q. Zhang, C. N. Cao, *J. Phys. Chem. B* **2005**, *109*, 15008; c) H. Park, W. Choi, *J. Phys. Chem. B* **2003**, *107*, 3885.

[17] S. C. Yan, S. B. Lv, Z. S. Li, Z. G. Zou, *Dalton Trans.* **2010**, *39*, 1488.

[18] a) V. Subramanian, E. E. Wolf, P. V. Kamat, *J. Am. Chem. Soc.* **2004**, *126*, 4943; b) J. Luo, P. A. Maggard, *Adv. Mater.* **2006**, *18*, 514.

[19] Y. Wang, R. Shi, J. Lin, Y. Zhu, *Energy. Environ. Sci.* **2011**, *4*, 2922.